Title

Permeability and Line-Tension-Dependent Response of Polyunsaturated Membranes to Osmotic Stresses

Journal

Biophysical Journal, 115(10)

ISSN

0006-3495

Authors

Emami, Shiva
Su, Wan-Chih
Purushothaman, Sowmya
et al.

Publication Date

2018-11-01

DOI

10.1016/j.bpj.2018.09.031

Peer reviewed

Biophysical Journal
Article

Biophysical Society

Permeability and Line-Tension-Dependent Response of Polyunsaturated Membranes to Osmotic Stresses

Shiva Emami,[1,3] Wan-Chih Su,[2] Sowmya Purushothaman,[1] Viviane N. Ngassam,[1] and Atul N. Parikh[1,2,3,4,*]
[1]Departments of Biomedical Engineering, [2]Chemistry, [3]Chemical Engineering, and [4]Materials Science & Engineering, University of California, Davis, California

ABSTRACT The lipidome of plant plasma membranes—enriched in cellular phospholipids containing at least one polyunsaturated fatty acid tail and a variety of phytosterols and phytosphingolipids—is adapted to significant abiotic stresses. But how mesoscale membrane properties of these membranes such as permeability and deformability, which arise from their unique molecular compositions and corresponding lateral organization, facilitate response to global mechanical stresses is largely unknown. Here, using giant vesicles reconstituting mixtures of polyunsaturated lipids (soy phosphatidylcholine), glucosylceramide, and sitosterol common to plant membranes, we find that the membranes adopt "janus-like" domain morphologies and display anomalous solute permeabilities. The former textures the membrane with a single sterol-glucosylceramide-enriched, liquid-ordered domain separated from a liquid-disordered phase consisting primarily of soy phosphatidylcholine. When subject to osmotic downshifts, the giant unilamellar vesicles (GUVs) respond by transiently producing well-known swell-burst cycles. In each cycle, the influx of water swells the GUV, rendering the membrane tense. Subsequent rupture of the membrane through transient poration, which localizes in the liquid-disordered phase or at the domain boundaries, reduces the osmotic stress by expelling some of the excess osmolytes (and solvent) before sealing. When subject to abrupt hypertonic stress, they deform by nucleating buds at the domain phase boundaries. Remarkably, this incipient vesiculation is reversed in a statistically significant fraction of GUVs because of the interplay with solute permeation timescales, which render osmotic stresses short-lived. This, then, suggests a novel control mechanism in which an interplay of permeability and deformability regulates osmotically induced membrane deformation and limits vesiculation-induced loss of membrane material. Interestingly, recapitulation of such dynamic morphological reconfigurability—switching between budded and nonbudded morphologies—due to the interplay of membrane permeability, which temporally reverses the osmotic gradient, and domain boundaries, which select modes of deformations, might prove valuable in endowing synthetic cells with novel morphological responsiveness.

INTRODUCTION

Cellular membranes of higher plants, a major class of sessile organisms, contain significant proportion of polyunsaturated phospholipids—those that contain at least one polyunsaturated fatty acyl tail (1). Because their nonrotating C=C double bonds are almost invariably separated by at least two saturated C-C bonds, these polyunsaturated fatty acid (PUFA) tails exhibit low energy barriers for conformational transitions (2). As a result, they switch readily between vastly different molecular shapes of similar energies, defying traditional classification based on fixed intrinsic shapes (e.g., conical, cylindrical, or inverted conical) and defined spontaneous molecular curvatures. This extraordinary conformational flexibility, fast adaptability, and shape plasticity confers plant cellular membranes containing PUFA-laden phospholipids with a distinct combination of physicochemical properties including enhanced lateral fluidity, high solute permeability (3), and low bending rigidities (4,5). Together, these characteristics facilitate a variety of specialized biological mechanisms—especially those that tend to stress the membrane—by lowering the costs of membrane deformations (5,6). Indeed, it has recently been shown using model membranes that polyunsaturated lipids facilitate membrane bending and fission by endocytic proteins (7)—the first step in the biogenesis of synaptic vesicles. Specifically, this study demonstrates that the presence of PUFA-containing lipids lowers the membrane-bending rigidity locally by adapting their conformation to membrane curvatures generated by the cooperative mechanical activity

Submitted May 17, 2018, and accepted for publication September 26, 2018.
*Correspondence: anparikh@ucdavis.edu
Shiva Emami and Wan-Chih Su contributed equally to this work.
Editor: Dimitrios Stamou.
https://doi.org/10.1016/j.bpj.2018.09.031

of two endocytic proteins—dynamin, a GTPase, which self-assembles on the membrane buds, and endophilin, a BAR-domain containing protein, which deforms and vesiculates the membrane—together promoting membrane fission.

These observations, highlighting the central roles of polyunsaturated lipids in promoting local, molecular-scale processes that deform the membrane (5,6), suggest a plausible hypothesis: the accumulation of polyunsaturated lipids in the cellular membranes of higher plants subject to frequent and harsh abiotic stresses (8), which tend to globally deform the membrane, confers an evolutionary benefit by facilitating stress response and adaptation. Although the cell wall is the outermost interface between the living protoplast and its surroundings, it is porous to small molecules (including many proteins) (9). As a consequence, the underlying solute-impermeable membrane—which is pressed against the cell wall because of the large hydrostatic, turgor pressure (0.2–5 Mpa, ~2–50 atm) (8)—effectively acts as the site where the environmental stress signals that determine plant response and adaptation are sensed, interpreted, and transduced (10). Specifically, increase in extracellular solute concentrations (8,11) subjects the plant cell to a hypertonic stress (12). This in turn triggers an instantaneous flow of water out of the cell (osmotic upshift), causing an instantaneous decrease in the cell volume (through the loss of water in vacuoles), reduction in turgor, and a shift in membrane tension. As a consequence, the plasma membrane deforms, and its interactions with the cell wall weaken. In a limiting case, when the hyperosmotic stress from the bath exceeds a certain threshold, plasmolysis—characterized by an essentially complete physical separation between the cell wall and the membrane with only a few plasma membrane protrusions, called Hechtian strands, linking the two—ensues (13). In the opposite scenario, in which the plant cell experiences a sudden drop in solute concentrations in the surrounding medium, the rapid influx of water (osmotic downshift) elevates the turgor pressure and stretches the membrane (14). This mechanical signal (i.e., membrane tension) is then converted into a chemical one, activating membrane channels (e.g., OSCA-1 and MSC-S) (15,16) or turning on a regulatory feedback loop between membrane tension and surface-area regulation such as through endocytic processes (17).

In addition to PUFA-laden phospholipids, plant plasma membranes also contain 1) a differentiated variety of sterols, including most abundantly sitosterol (Sito), stigmasterol, and campesterol (18); and 2) chemically distinct classes of plant sphingolipids (e.g., GlcCers and GIPCs) (19). By contrast, mammalian (or fungal) plasma membranes contain only one major sterol, namely cholesterol (animal cells) and ergosterol (fungal cells), and sphingomyelin represents their dominant sphingolipid. This compositional diversity of plant membranes allows unique intermolecular interactions and self-assembly of molecules, giving rise to dynamic domain structures (20) that are distinct from animal or fungal membranes. Taken together, the essential lipid mixtures of plant origin—combining the conformational adaptability of PUFA-containing phospholipids with physical properties of sterols and sphingolipids—thus feature a unique combination of permeability, deformability, and spatial and molecular organization. But how these physicochemical properties collaborate in determining the responsiveness of plant membranes to global osmotic stresses is largely unknown.

In the work reported here, we used synthetic membranes reconstituting a mixture of polyunsaturated lipids and a sterol of plant origin. Specifically, we reconstituted soy phosphatidylcholine (Soy-PC), Sito, and glucosylceramide (GlcCer) in giant unilamellar vesicles (GUVs) and characterized their lateral organization, solute permeabilities, and osmotic-stress-induced morphological deformabilities. We find that these membranes display a striking lateral phase separation into a sterol-enriched liquid-ordered (L_o-like) and sterol-depleted liquid-disordered (L_d-like) phase characterized by a single, macroscopic domain and display enhanced permeabilities for water as well as larger solutes such as glucose. When subject to hypotonic stress, these vesicles relax through well-known swell-burst cycles. Here, a cascade of transient pores—either at the phase boundaries or in the L_d-like phase—synchronized with a transient budding eject the excess osmolyte from the vesicular interior in a stepwise manner. When subject to osmotic deflation through an abrupt exposure to hypertonic stress, the GUVs deform by inducing curvatures and nucleating buds at the domain phase boundaries. This incipient budding transition, remarkably, divides into a subpopulation in which the buds reabsorb into the mother vesicle and another in which buds mature into daughter vesicles. These results reflect a complex interplay of membrane permeability and deformability mediated by phase boundary forces and plausibly suggest new roles of polyunsaturated phospholipids in regulating membrane deformations and limiting membrane loss under osmotic stresses.

MATERIALS AND METHODS

Materials

L-α-phosphatidylcholine (Soy-PC), Sito, GlcCer, 1-palmitoyl-2-oleoyl-*sn*-glycero-3-phosphocholine (POPC), 1,2-dilinoleoyl-*sn*-glycero-3-phosphocholine, and lissamine rhodamine B 1,2-dioleyl-*sn*-glycero-3-phosphoethanolamine (Rho-B DOPE) were acquired from Avanti Polar Lipids (Alabaster, AL). Glucose was obtained from Sigma-Aldrich (St. Louis, MO), and 2-NBDG (2-(N-(7-Nitrobenz-2-oxa-1,3-diazol-4-yl)Amino)-2-Deoxyglucose) (NBD-glucose) was purchased from Thermo Fisher Scientific (Eugene, OR). Sucrose was obtained from EMD Chemicals (Philadelphia, PA). Chloroform was purchased from Thermo Fisher Scientific (Waltham, MA). Head-labeled N-(7-nitrobenz-2-oxa-1,3-diazol-4-yl)-1,2-dihexadecanoyl-sn-glycero-3-phosphoethanolamine, triethylammonium salt (NBD-PE) was purchased from Life Technologies (Carlsbad, CA). All chemicals were used without further purification. Glass-bottom, eight-well plates were obtained from MatTek (Ashland, MA). Indium tin oxide (ITO)-coated glass slides (resistance 4–30 U) were obtained from Delta Technologies (Loveland, CO). Lipid nomenclature is as follows: DLiPC, 1,2-dilinoleoyl-*sn*-glycero-3-phosphocholine;

PLiPC, 1-palmitoyl-2-linoleoyl-*sn*-glycero-3-phosphocholine; OLiPC, 1-oleoyl-2-linoleoyl-*sn*-glycero-3-phosphocholine; SOPC, 1-stearoyl-2-oleoyl-*sn*-glycero-3-phosphocholine; LiLnPC, 1-linoleoyl-2-linolenoyl-*sn*-glycero-3-phosphocholine; DPPC, 1,2-palmitoyl-*sn*-glycero-3-phosphocholine; DOPC, 1,2-dioleoyl-*sn*-glycero-3-phosphocholine; GIPCs, glycosyl inositol phosphoryl ceramides.

Preparation of GUVs

GUVs were prepared by electroformation according to a published protocol (21,22). Briefly, we began by preparing stock solutions consisting of the desired molar composition of lipid components (Soy-PC, Sito, and GlcCer, 2:2:1 and 3:1:1) in chloroform at 2 mg/mL. Experiments were performed by doping the GUVs with trace concentrations of single-labeled lipids, which included Rho-B DOPE (1%) or NBD-PE (3%) to fluorescently label both L_d-like and L_o-like phases in raft mixtures. In all cases, small droplets (15–30 μL) of stock solution were spread on the conductive side of each of two ITO-coated slides (4–30 Ω) as the chloroform evaporated. The slides were then further dried in a vacuum desiccator overnight. A chamber was formed by sandwiching a 1-mm-thick rubber O ring (Ace Hardware, Davis, CA) sealed with high-vacuum grease (Dow Corning, Midland, MI) between the conductive sides of the two ITO-coated slides. After the ring was attached to one of the slides, the dried film was hydrated with 300 mM sucrose solution in deionized water at room temperatures (exceeding effective T_m of the lipid mixtures). The second ITO-coated slide was placed over the ring, sealing the chamber and ensuring that no visible air bubbles were trapped inside. Using a function generator, a 4.0 V (pp) alternating current sine wave was applied across the two slides at 10 Hz for 1–2 h, followed by a 4.0 V (pp) square wave at 2 Hz for 1–2 h, producing GUVs of highly reproducible quality and yielding a high abundance of 5 to 50-μm-sized GUVs. During the formation of GUVs, the chamber was covered to protect from light. After GUV formation was observed, the ITO formation chamber was disassembled, and the solution containing GUVs was pipetted off and used immediately or stored in small centrifuge tubes at 4°C. Vesicles were used within a week of preparation.

Spinning disk confocal fluorescence microscopy

Spinning disk confocal fluorescence microscopy measurements were performed using an Intelligent Imaging Innovations Marianas Digital Microscopy Workstation (3i, Denver, CO) fitted with a CSU-X1 spinning disk head (Yokogawa Musashino-shi, Tokyo, Japan) and a QuantEM 512SC EMCCD (electron-mulitplying charge-coupled device) camera (Photometrics, Tuscon, AZ). Fluorescence micrographs were obtained using oil immersion objectives (Zeiss Fluor 40× (numerical aperture, NA 1.3), Zeiss Plan-Fluor 63× (NA 1.4), and Zeiss Fluor 100× (NA 1.46); Carl Zeiss, Oberkochen, Germany). Samples of osmotically balanced GUVs were prepared as described in the previous section. In a typical experiment, the glass-bottom eight-well plate containing osmolyte-laden solution was mounted onto the microscope, and once oiled, the objectives were raised to form a meniscus between the cover glass and the objective. To impose osmotic gradients in real time, GUV suspension was added to the solution in the sample chambers. Rho-B DOPE (Ex/Em; 560/583) was exposed with a 5 mW 561 laser line. NBD-PE (Ex/Em; 460/535) and 2-NBDG (Ex/Em; 465/540) were exposed with a 5-mW 488 laser line. The images were subsequently analyzed using ImageJ (http://rsbweb.nih.gov/ij/), a public-domain software, and Slidebook digital microscopy imaging software (3i).

Fluorescence microscopy

Wide-field epifluorescence measurements were carried out using a Nikon Eclipse TE2000S inverted fluorescence microscope (Technical Instruments, Burlingame, CA) equipped with a Roper Cool Snap camera (Technical Instruments), an Hg lamp as the light source, and filter cubes to filter absorption and emission to the source and the CCD camera, respectively. Videos were taken using a Plan Fluor 20× (NA, 0.25) objective (Nikon, Tokyo, Japan). Rho-B DOPE (Ex/Em; 560/583) is exposed using a 561 laser line. NBD-PE (Ex/Em; 460/535) and 2-NBDG (Ex/Em; 465/540) were exposed using a 488 laser line.

FRAP experiments

Fluorescence recovery after photobleaching (FRAP) experiments were performed with a 5-mW 561 laser line or a 5-mW 488 laser line. Vesicles were viewed in the equatorial plane with a 63× objective and a Quantem512SC EMCCD (electron-multiplying charge-coupled device) camera, giving a 512 × 512 pixel image. Rho-B DOPE and NBD-PE fluorescent probes were bleached in a rectangular region along the contour of the GUV (7 μm long) at 100% of maximal laser power. Recovery of fluorescence was recorded and measured from the subsequent 45–100 frames, two frames per second. The fluorescence recovery of each vesicle was fit to the following equation: $I(t) = I_0 + a(1 - e^{-bt})$, where I is the normalized fluorescent intensity and t represents time. The fitting enabled us to estimate the half-time $(\tau_{1/2})$ for recovery. The diffusion coefficient was calculated as $D = 0.224 \times r^2/\tau_{1/2}$, where r is the radius of the bleached spot and $\tau_{1/2}$ is the half-time of recovery (23).

Membrane leakage assay

GUVs were prepared as described above, with mixtures consisting of Soy-PC/Sito/GlcCer (2:2:1) labeled with Rho-B DOPE (1%) and NBD-PE (3%). Vesicles were formed with 300 mM sucrose and immersed in medium containing 100, 300, or 500 mM glucose solution with 58 μM 2-NBDG. Red and green channels were simultaneously monitored to observe any leakage of the 2-NBDG across GUV membranes into the vesicle interior.

Phase-contrast microscopy measurements

For all the measurements, Nikon T2000 phase-contrast inverted microscope with a 20× objective was used. GUVs were prepared in 150 mM sucrose solution as described in Methods. 2 μL of GUVs were then suspended into 200 μL of 150 mM glucose solution for viewing under phase contrast setup. The change in the intensity at the interior of the vesicle was recorded using photonic sciences Camera (CoolSNAP HQ CCD camera, A04K881007; Photonic Sciences Camera, Robertsbridge, UK) at the rate of 2 s per frame.

Calculation of permeability

To calculate the permeability of the membrane to glucose, the radius of the vesicle and the intensity at the center of the vesicle were determined using an in-house MATLAB routine. Once the coordinates of the center are obtained, a 5 × 5 pixel square around the center is used to calculate the average intensity at the center. The intensity is normalized by calculating average intensity of 5 × 5 pixel square at an empty site in the frame. The value of the radius is obtained using the edge detection algorithm in MATLAB after performing Otsu threshold on all the frames. The permeability values were then obtained using the values of the initial intensity, the final intensity, and the radius of the vesicle (see Supporting Materials and Methods).

RESULTS

We begin with the preparation of GUVs (20–50 μm in diameter) by adopting the standard electroformation method

(22,24) (Materials and Methods). For study, we used binary and ternary mixtures containing three major classes of plant plasma-membrane lipids: Soy-PC, GlcCer ($T_m \sim 87°C$), and Sito ($T_m \sim 136–140°C$) (Fig. 1 *A*) (25). Our primary compositions included Soy-PC/Sito/GlcCer in two molar ratios, namely 2:2:1 and 3:1:1, mimicking two of the most common lipid ratios in typical plant cells (26). The Soy-PC itself is a mixture of a number of distinct lipid species of varying degrees of acyl tail unsaturation (e.g., dipolyunsaturated and saturated-polyunsaturated species) including DLiPC (~41%, $T_m \sim -57°C$, 18:2, 18:2), PLiPC (~27%, $T_m \sim -15°C$, 16:0, 18:2), OLiPC (~15%, $T_m < 0°C$, 18:1, 18:2), LiLnPC (~3.7%, $T_m < 0°C$, 18:2, 18:3), PLnPC (~1.3%, 16:0, 18:3), SLiPC (~2.4%, $T_m \sim -16°C$, 18:0, 18:2), SOPC (~5%, T_m ~6°C, 18:0, 18:1), and a residual concentration of fully saturated DPPC (~3.5%, T_m ~41°C, 16:0, 16:0) (Materials and Methods) (27). Note that roughly 90% of Soy-PC components contain PUFA-containing phospholipids, of which ~45% have both PUFA acyl tails. To enable visualization by fluorescence microscopy, our GUVs are doped with a low concentration of fluorescently labeled probe lipids, namely Rho-B DOPE (1 mol%) and/or NBD-PE (3 mol%). In all cases, the GUVs encapsulate 300 mM sucrose, and they are immersed in sucrose (or glucose) solutions of varied osmolarities.

Biphasic liquid-liquid phase separation of multicomponent plant lipid mixtures

We begin by visualizing a collection of single GUVs consisting of an equimolar two-component mixture of Soy-PC and Sito (sans GlcCer) containing 300 mM sucrose and bathed in 300 mM glucose (or sucrose) using spinning disk confocal fluorescence microscopy. Strikingly, virtually all GUVs reveal a binary pattern of fluorescence emission consisting of a single, micrometer-scale domain, indicating a large-scale phase separation (Fig. 1 *Bi*). The two fluorescently labeled probe lipids used here, namely Rho-B DOPE and NBD-PE, have complementary phase-sensitive partitioning preferences. The former stains the sterol-depleted and less dense L_d-like phases, and the latter partitions into the sterol-enriched, denser L_o-like phase (28).

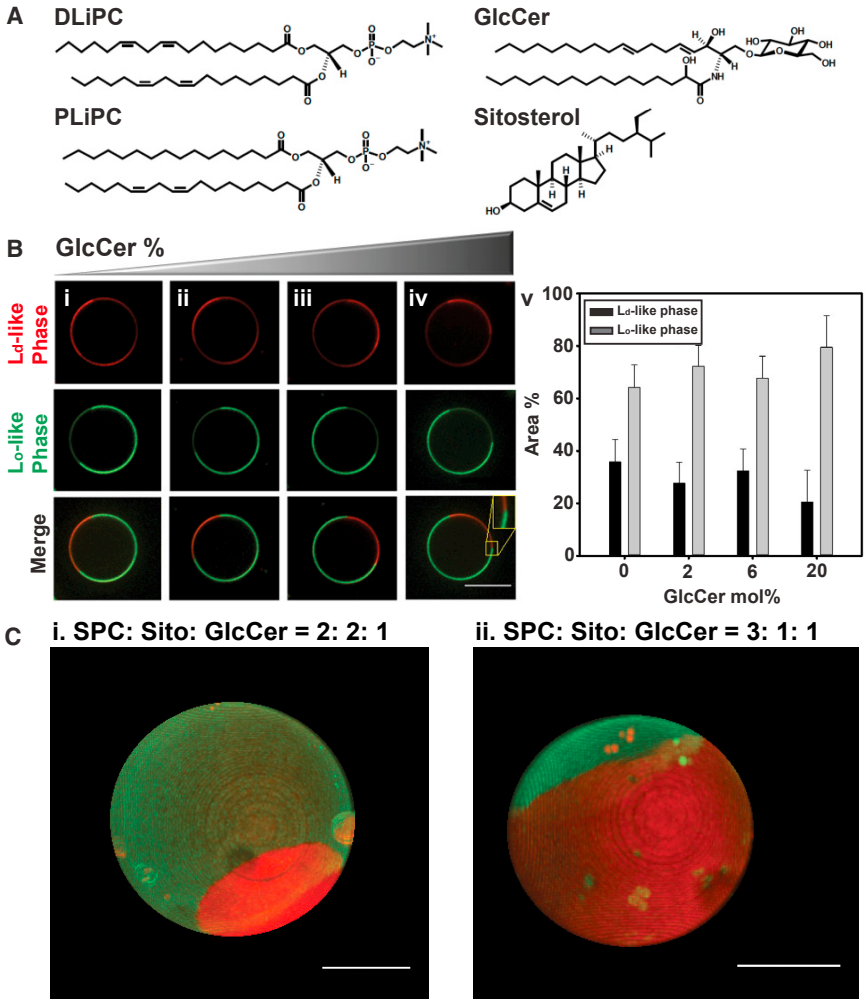

FIGURE 1 Biphasic liquid-liquid phase separation of multicomponent plant lipid mixtures produces monodomain morphologies. (*A*) The chemical structures of two of the most abundant lipids in Soy-PC, one plant GlcCer species, and Sito; (*B*) (*i–iv*) confocal fluorescence images at the equatorial plane of GUVs prepared using equimolar Soy-PC and Sito with varying amounts of GlcCer from (*i*) 0% to (*ii*) 2%, (*iii*) 6%, and (*iv*) 20%. Scale bars, 15 μm. (*v*) The area fraction of the two coexisting phases. (*C*) Three-dimensional stacks of confocal fluorescence images of GUVs composed of Soy-PC, Sito, and GlcCer in ratios of (*i*) 2:2:1 and (*ii*) 3:1:1. Both ratios produce "janus-like" morphologies. Scale bars, 20 μm. All GUVs encapsulate 300 mM sucrose solution and are suspended in iso-osmolar medium containing 300 mM glucose. All GUVs are doped with L_d-phase-sensitive Rho-B DOPE (1 mol%, *red*) and L_o-phase-sensitive NBD-PE (3 mol%, *green*) dyes. All measurements were taken at room temperature (24°C). To see this figure in color, go online.

Thus, the observed binary pattern of fluorescence indicates that Sito does not distribute uniformly within the Soy-PC bilayer but rather laterally segregates Soy-PC components, producing coexisting sterol-rich and sterol-depleted phases. Furthermore, because Soy-PC itself is a heterogeneous mixture of many phospholipids (see above), the appearance of fluid phase domains suggests that Sito sorts the mixture. In analogy with the behavior of cholesterol in mammalian cells, it seems likely that Sito partitions preferentially with saturated and hybrid (single-PUFA-tail) lipids (e.g., DPPC and PLiPC), producing a condensed L_o-like phase while isolating more unsaturated, dipolyunsaturated lipid species (e.g., DLiPC) into a separate, L_d-like phase. This is corroborated by an independent control experiment in which we replaced the Soy-PC mixture by a simple binary mixture of polyunsaturated and monounsaturated phospholipids. Specifically, we used DLiPC lipid (30%) (18:2, 18:2) and POPC (16:0, 18:1, 20%) together with ~50% Sito. Here, too, single large microscopic domains (Supporting Materials and Methods; Fig. S1) decorate the vesicular boundary, confirming that Sito alone is sufficient to sort mixtures of dipolyunsaturated and monopolyunsaturated lipids.

Introducing different proportions of GlcCer (2, 6, and 20%) into the equimolar Soy-PC and Sito mixtures above retains the qualitative membrane structure described: taut spherical GUVs with fully segregated, twin coexisting liquid phases characterized by single microscopic domains (Fig. 1, *B*ii–Biv, and *C*; Supporting Materials and Methods; Fig. S2). This confirms that GlcCer, a high-melting lipid component, does not segregate from the phospholipid-sterol mixtures to produce a separate gel phase but rather mixes with the existing L_o-like phase of the binary Soy-PC-Sito mixtures above. It is important to note here that the low concentrations of GlcCer, comparable to that of the fluorescent probes, should not complicate our findings because it partitions between macroscopic coexisting phases produced largely by the sorting of Soy-PC mixtures in the presence of Sito. In all of the cases above, domain boundaries display smooth arcs of circular segments consistent with the fluid nature of the domains, which is independently verified using FRAP measurements in confocal microscopy mode for each of the two coexisting phases (Fig. 2; Videos S1 and S2). A simplified analysis of the recovery profile (23) yields diffusion coefficients of 0.34 ($\pm$0.1 SD) $\mu m^2/s$ and 1.37 ($\pm$0.1 SD) $\mu m^2/s$ for the L_o-like and L_d-like phases respectively—consistent with those expected for sterol-enriched and fluid phases, respectively (29).

To confirm that Sito fluidizes higher melting components of the lipid mixture, we also prepared GUVs consisting of a binary mixture of Soy-PC/GlcCer (molar ratio 3:1). Here, the membrane texture matches well with the expected coexistence of a fluid and solid (L_d-like/*S*) phases with the *S* phase, presumably composed primarily of higher-melting GlcCer, exhibiting irregular boundaries (Supporting Materials and Methods; Fig. S3 A). After incorporation of 10 or 20% of Sito into this mixture, the domain morphologies change to more rounded, circular domains, suggesting that the *S* phase coexistence is replaced by a fluid one, producing coexisting L_d-like and L_o-like fluid phases (Supporting Materials and Methods; Fig. S3, B and C). This lends further support to the foregoing inference that Sito preferentially partitions with the less unsaturated lipids among the existing lipids.

In sum, the observations above indicate that the membranes of GUVs reconstituting mixtures of PUFA-containing phospholipids readily phase separate into two coexisting fluid phases (30): 1) a sterol-depleted L_d-like phase segregating poly(unsaturated) Soy-PC; and 2) the sterol-enriched denser phase (L_o-like), which accumulates both the less unsaturated components of Soy-PC and, when present, GlcCer. This biphasic nature of the phase-separated membrane, characterized by liquid-liquid coexistence, parallels the observations of L_o and L_d phases in cholesterol-containing ternary lipid mixtures (31) and more complex plasma-membrane vesicles (32).

Janus morphologies of phase-separated membrane domains

A noteworthy feature of the coexisting fluid phases in the plant lipid GUVs above is the macroscopic nature of their phase segregation. Unlike cholesterol-containing models of animal cell membranes (e.g., ternary lipid mixtures containing DOPC, cholesterol, and sphingomyelin)—in which an "emulsion" consisting of multiple microscopic domains most frequently textures the membrane—Sito-containing membranes demix primarily into fully segregated single spheroidal domains (>90%, $n = 100$), producing "janus-like" morphologies (Fig. 1, B and C): the two opposing and immiscible "faces" of these membranes correspond to single domains of L_o-like and L_d-like coexisting liquid phases. This approach to the macroscopic phase separation suggests a strong influence of phase boundary forces.

Solute permeabilities of plant membrane GUVs

To characterize the permeability properties of Soy-PC/Sito/GlcCer membranes, we conducted the standard leakage assay using fluorescence microscopy. Immersing GUVs enveloped by Soy-PC/Sito/GlcCer membranes together with those bounded by POPC (as a reference) in a bath containing glucose doped with a small concentration (~1.5 mol%) NBD-PE-labeled glucose, we found rapid permeation of labeled glucose across the plant membrane vesicles and little or no permeation across POPC vesicles during the experimental timescales. Note this rapid glucose transport across plant membrane vesicles occurs under all conditions of osmotic balance, including isotonic, hypertonic, and hypotonic baths (Fig. 3 *A*; Videos S3, S4, and S5). This simple

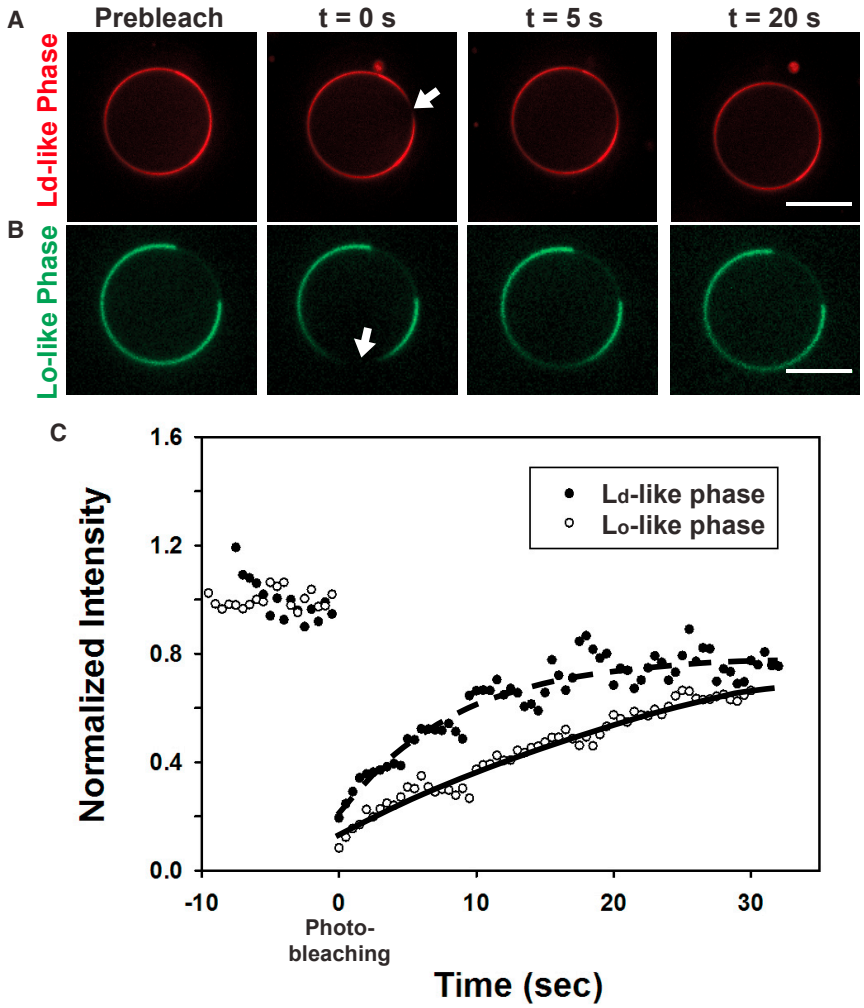

FIGURE 2 Fluorescence recovery after photobleaching (FRAP) measurements to determine the fluidity of two coexisting phases. Selected frames from a time-lapse sequence of FRAP measurements at the L_d-like and L_o-like phases of a single GUV consisting of Soy-PC/Sito/GlcCer (2:2:1) are shown. (*A*) FRAP of the L_d-like phase and (*B*) FRAP of the L_o-like phase. Fluorescence intensity was monitored before and immediately after the photobleaching. Here, four representative time points including prebleach, at the onset of photobleaching (0 s), during recovery (5 s), and ~95% of the recovery (20 s) are shown. Arrows highlight the bleached regions. Scale bars, 15 μm. (*C*) Normalized fluorescence recovery profiles of the L_d-like phase and L_o-like phase calculated by measuring the average intensity of the photobleached area after background subtraction. Lines represent the exponential fits of experimental profiles to derive diffusion coefficients (see Materials and Methods for details). To see this figure in color, go online.

test suggests that these model membranes containing high fractions of PUFA-laden lipids facilitate ready passage of glucose (and labeled glucose).

To quantify glucose permeabilities, we monitored the phase contrast of sucrose-laden GUVs (150 mM) immersed in isotonic glucose solution. Because the refractive index of sucrose solution is higher than that of glucose solution at comparable concentrations and because the contrast varies linearly with the concentration difference of the diffusible solute(s), time-dependent changes in the phase contrast can be used to identify and quantify the permeability of the diffusible solute. For GUVs bounded by Soy-PC/Sito/GlcCer (2:2:1) membranes, these measurements reveal a rapid change in the intensity of the sucrose-laden interior, resulting in a diminution in the optical contrast suggesting high permeability for glucose across the vesicular boundary. By contrast, control experiments using GUVs consisting of POPC membranes reveal significantly less pronouced changes in the phase contrast during the experimental timescales (Fig. 3, *B* and *C*; Videos S6 and S7). Furthermore, by analyzing the time-dependent changes in the phase contrast, membrane permeability for glucose can be readily determined (33):

$$P = -\left(\frac{R}{3t}\right) ln(\Delta I_t - \Delta I_0 + 1),$$

where P is the permeability coefficient, R is the radius of the vesicle, and ΔI_t and ΔI_0 are the normalized intensities at the measurement time t and initial time $t = 0$ (Supporting Materials and Methods, Section 2). Following this analysis, we estimate the glucose permeability coefficient of Soy-PC/Sito/GlcCer (2:2:1) to be 5.57 ($\pm$ 1.31 SD) $\times 10^{-7}$ cm/s—roughly two orders of magnitude higher than that of POPC GUVs (3.76 ($\pm$ 1.20 SD) $\times 10^{-9}$ cm/s) (34) and previous reports of glucose permeabilities of lipid extracts of human red blood cells, cholesterol, sphingomyelin, and PC mixtures (~6–25 $\times 10^{-9}$ cm/s) (35,36). The high permeability of our PUFA-laden mixtures translate into the characteristic relaxation times, $t = R/3P$, of ~9 min (Soy-PC/Sito/GlcCer 2:2:1 membranes), considerably smaller than >20 h for mammalian lipid fractions for representative GUVs 10 μm in radius.

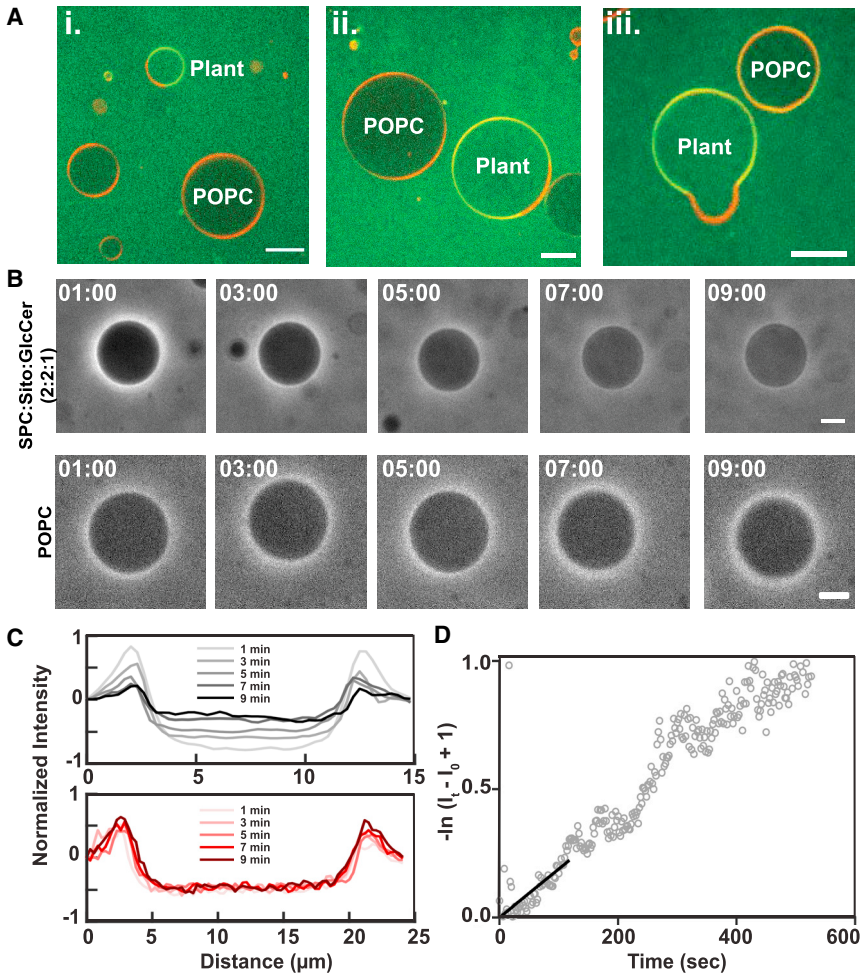

FIGURE 3 Dye leakage assays to quantify selective permeability of plant lipid GUVs for glucose. (*A*) Confocal fluorescence images taken at ~1 min after immersion in the fluorescently labeled glucose solution reveal rapid leakage of glucose in plant GUVs (2:2:1 Soy-PC/Sito/GlcCer labeled with 1% Rho-B DOPE and 3% NBD-PE) but little or no permeation in POPC (labeled with 1% Rho-B DOPE) GUVs. GUVs are immersed in (*i*) hypotonic (ΔC = 200 mM), (*ii*) isotonic (ΔC = 0 mM), and (*iii*) hypertonic (ΔC = 200 mM) external medium doped with 58 μM fluorescently labeled 2-NBD glucose. Scale bars, 10 μm. (*B*) Selected frames from a time-lapse sequence of phase-contrast images of plant lipid GUVs (*top row*) and POPC GUVs used as controls (*bottom row*). GUVs were made in 150 mM sucrose solution and suspended in 150 mM of iso-osmolar glucose solution. Scale bars, 10 μm. Time stamps are shown as minutes:seconds. (*C*) Intensity profiles at the equatorial plane of plant (*top, gray*) and POPC (*bottom, red*) GUVs. (*D*) Measurement of permeability of plant vesicles obtained by recording decrease in phase-contrast intensity at the center of the vesicle. To see this figure in color, go online.

Taken together, the experiments above suggest that giant vesicles' Soy-PC/Sito/GlcCer lipids phase separate, producing large, macroscopic monodomain morphology, and exhibit significantly higher solute permeability for glucose. As a consequence, sucrose-laden vesicles in glucose-containing surroundings experience an unusual combination of permeable (glucose) and impermeable (sucrose) solutes, setting the stage for a complex response to osmotic imbalances, such as presented below.

Dynamic response to osmotic downshift

To address how these GUVs displaying single domains respond to sudden osmotic insults, we monitored the behaviors of a suspension of vesicles consisting of a ternary mixture of Soy-PC/Sito/GlcCer (2:2:1 and 3:1:1 mol ratios) containing 300 mM sucrose in an extravesicular dispersion medium containing 100 mM sucrose (or glucose).

The time-lapse videos (Videos S8, S9, and S10) and a montage of selected frames of confocal fluorescence micrographs (Fig. 4) document the vesicular response. These data reveal several noteworthy features. First, immediately after immersion into a hypotonic bath, the size of individual GUVs begins to pulsate: the vesicle diameter gradually grows up to a limiting size, at which point it abruptly shrinks (by ~3–5% in diameter). This oscillatory swell-shrink behavior repeats multiple times ($n > 15$), persisting over tens of minutes. Second, the period of oscillation increases with the passage of time or the cycle number. The cycle period—defined as the time elapsed between two consecutive instances of full swelling—increases severalfold over 15 min. Third, coincident with the onset of each shrink regime, single microscopic pores transiently appear, the lifetimes of which are short (hundreds of milliseconds), comparable to the temporal resolution of ~300 ms in our measurements. These observations are fully consistent with previous experimental reports and theoretical predictions (37–42) revealing that single GUVs respond to hypotonic stress through characteristic swell-burst cycles (43,44). An osmotically triggered influx of water swells the GUVs, increasing their sizes. Consequent stretching of the membrane boundary irons out their thermally excited undulations and renders the membrane boundary tense. Beyond a threshold tension, membranes lyse by opening

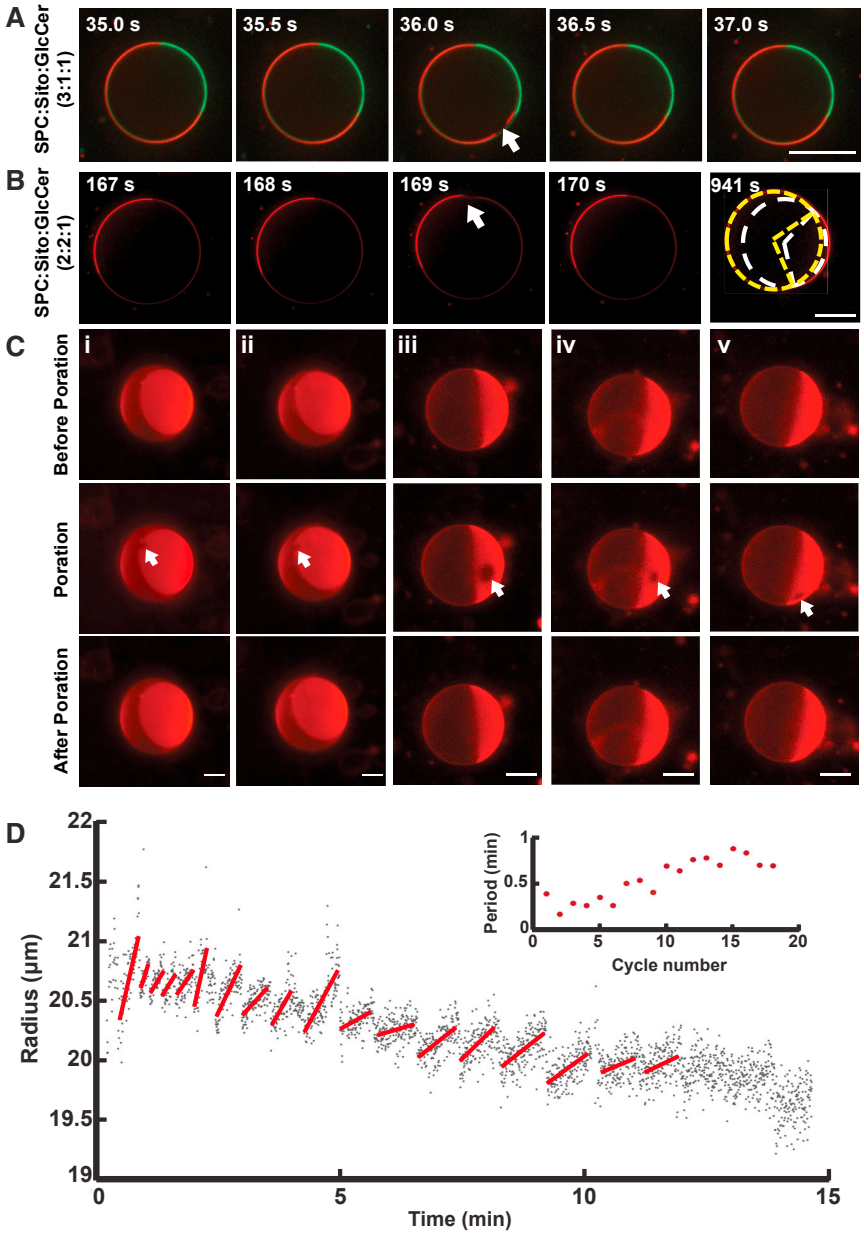

FIGURE 4 Plant lipid GUVs exposed to osmotic downshifts exhibit characteristic swell-burst cycles. Selected frames from a confocal time-lapse sequence of GUVs containing 300 mM sucrose suspended in 100 mM glucose solution are shown, revealing the appearance of microscopic pores and pinch ((*B*) 941 s) either at the boundary of L_d-like and L_o-like phases or in the L_d-like phase during swell-burst cycle. Arrows highlight the pores. Dashed circles represent different curvatures of L_o-like and L_d-like phases. Scale bars, 20 μm. (*C*) A wide-field fluorescence micrograph of GUVs revealing five arbitrarily selected instances of pore formation during swell-burst cycles. Scale bars, 10 μm. (*D*) Oscillations in vesicle radius during swell-burst cycles of a representative GUV. The inset shows the time between each swell and burst cycle measured from the time of highest and lowest points of the fitted data in the plot between each event. The GUVs are composed of Soy-PC, Sito, and GlcCer in molar ratios of (*A*) 3:1:1 and (*B–D*) 2:2:1 doped with 1% Rho-B DOPE and 3% NBD-PE. To see this figure in color, go online.

microscopic pores, which relieves the membrane tension. Consequently, the efflux of solute (and solvent) through the pores lowers the osmotic pressure difference, which then drives pore closure. This swell-burst process reiterates in a negative feedback loop, reducing osmotic gradient in a stepwise manner until the sublytic osmotic pressure is reached.

Additionally, our experiments reveal features unique to GUVs displaying janus monodomain morphologies. First, we find that the domain sizes do not change during swell-burst cycles. Previously, we and others have shown that homogeneous GUVs consisting of phase-separating lipid mixtures exhibit a coupling of swell-burst cycles with the membrane's domain texture (41,42): tense membranes of swollen vesicles promote phase-separated states characterized by large microscopic domains, whereas porated membranes during the burst phase break up and disperse the domains, presumably into nanoscopic domains below the resolution of our microscopic experiments. Thus, the pulsatory swell-burst cycles also produce corresponding oscillations in membrane mixing-demixing behavior. Our observations that the domain texture remains unperturbed during the oscillatory swell-burst cycles suggest the preponderance of line tension. Even in the absence of applied membrane tension, the janus vesicles organize the coexisting phases to adopt the smallest interface length between

the coexisting phase. Thus, it seems reasonable that introduction of membrane tension during the swell phase does little to the existing domain morphologies.

Second, we find that the spatial locations of pore formation are not random. Pores form either 1) at the phase boundaries separating L_o-like and L_d-like phases when the L_d-like is a minority phase (i.e., Soy-PC/Sito/GlcCer at 2:2:1 mol ratio) or 2) in the L_d-like phase when the L_d-like phase assumes an areal majority (i.e., Soy-PC/Sito/GlcCer at 3:1:1 mol ratio). This phase preference for the L_d-like phase and phase boundaries corroborates predictions from previous molecular simulations (45) and a more recent experimental observation of the phase preference of electrically induced membrane pores (46). In all of these cases, the kinetics of pore formation can be viewed in terms of the transient aqueous pore hypothesis, which implicates the energy barrier for the transition between a fluctuation-mediated hydrophobic pore and a toroidal one stabilized by lipid reorientation at the pore boundaries forming a hemimicellar edge. The lowered energy barrier for this transition in the L_d-like phase and at phase boundaries can then be readily reconciled in terms of their biophysical attributes: the L_d-like phase enriched in PUFA-containing flexible lipids (as well as phase boundaries) are more heterogeneous in composition, less cohesive in lateral packing, thinner in hydrophobic thickness, and offer lower local bending rigidity compared to the L_o-like phase.

Dynamic response to osmotic upshift

To explore how the plant-lipid-containing GUVs with janus membranes respond to sudden osmotic upshifts, we next transferred a suspension of GUVs of ternary mixture of Soy-PC/Sito/GlcCer (2:2:1 and 3:1:1 mol ratios) containing 300 mM sucrose into an extravesicular dispersion medium containing 500 mM glucose. The transvesicular hypertonic osmotic stress, which corresponds to the osmolyte concentration difference (200 mM), initiates an instantaneous vesicular response. The time-lapse videos of confocal fluorescence microscopy (Fig. 5, *A–C*) illustrates the highly reproducible ($n = 15$) dynamics that ensue upon the application of the hypertonic stress to GUVs consisting of Soy-PC/Sito/GlcCer at 2:2:1 (Videos S11 and S12) and 3:1:1 (Video S13) mole ratios. Immediately after subjecting the GUV to a deswelling osmotic stress, the nearly perfectly spherical morphology of the GUV is quickly abandoned (~10–30 s), replaced by one characterized by a single bud. The bud, delineated by the domain phase boundary, contains the minority domain in its entirety and protrudes away from the parent vesicle: for the Soy-PC/Sito/GlcCer ratio of 2:2:1, the minority L_d-like phase buds, and the budding occurs for the L_o-like phase for the corresponding lipid ratio of 3:1:1. In both cases, the deformed interface in the neck region reveals that the L_d-like domain bends toward the L_o-like domain (Fig. 5, *D* and *E*), consistent with the expected smaller bending rigidities of L_d-like domains compared to L_o-like domains (47,48).

Examining more than 30 different GUVs, we find that this initial response bifurcates into two distinctly different trajectories of shape evolution. In the majority of the cases (~70%), the bud formation is transient and fully reversed. The bud forms within the first 10–30 s after imposition of the osmotic differential, then gradually pulls back to the curvature of the mother GUV, returning to the initial

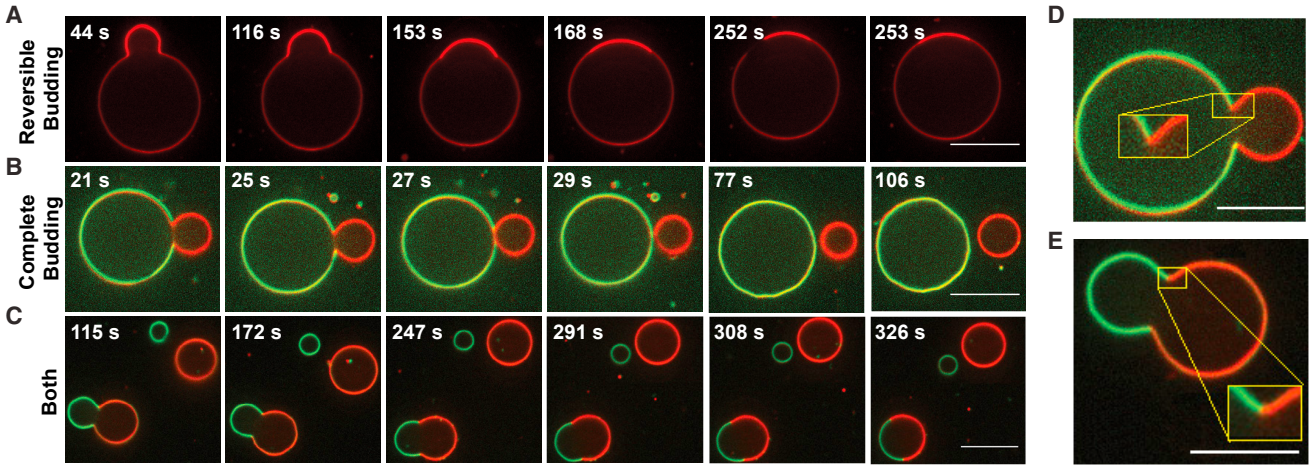

FIGURE 5 Response of plant lipid GUVs to osmotic upshift includes both reversible as well as irreversible budding. Selected frames from time-lapse videos of confocal fluorescence microscopy images of single GUVs containing 300 mM sucrose upon immersion in the external dispersion medium containing 500 mM glucose are shown, in which (*A*) reversible budding, (*B*) complete budding, and (*C*) both reversible and complete budding occur with equal probability. The GUVs are composed of Soy-PC, Sito, and GlcCer in a ratio of either (*A* and *B*) 2:2:1 or (*C*) 3:1:1 and doped with 1% Rho-B DOPE and 3% NBD-PE. Scale bars, 20 μm. (*D* and *E*) The deformed interface in the neck region reveals that the L_d-like phase bends toward the L_o-like phase in (*A*) and (*B*) and (*C*) cases, respectively. Scale bars, 15 μm. To see this figure in color, go online.

spherical state (~60–300 s depending on the size of the bud), which persists in the steady state for the length of the experimental time (≥15 min). In the remaining 30% of the cases, the initial bud continues to mature, characterized by the rapid rounding of the bud and concomitant reduction in the diameter of the neck connecting the bud to the mother. The process culminates with the formation of a fully spherical bud that separates away, pinching off from the mother vesicle and producing a daughter vesicle of only the minority of the two coexisting phases (either L_d-like or L_o-like depending on the membrane composition and domain size) of the parent vesicle. After the complete budding (typically 40–60 s after the application of the osmotic stress), the mother vesicle begins to display rather pronounced flickering—independent of whether it contains the majority L_d-like or the L_o-like phase—reflecting significantly reduced membrane tension.

Lipid bilayers containing PUFA-laden lipids are susceptible to oxidation, especially in the membranes containing fluorescent molecules, which are prone to photo-oxidation. To confirm that the unusual budding dynamics we witness do not arise from artifacts such as lipid oxidation (49) or optical tweezing (50), we carried out additional experiments (see Supporting Materials and Methods, Section 3). These experiments confirm that under the illumination conditions we used (5 mW power, 1–3 mol% of fluorescently labeled lipids), there were little or no measurable deformations in the membrane shape ($n = 5$). By contrast, when we illuminated the GUVs using much higher optical illumination power (>50 mW), we found irreversible shape deformations, which included budding and division (Videos S14 and S15).

DISCUSSION

Distinct from their mammalian counterparts, membranes of higher plants have evolved a rich molecular diversity in their lipidome, which also changes with the environmental stress conditions. Characterizing giant vesicles, which reconstitute dominant plant plasma membrane lipids—namely conformationally plastic polyunsaturated mixtures of phospholipids in Soy-PC, GlcCer, and Sito—we found two major differences in their biophysical properties from their mammalian counterpart models containing monounsaturated lipids (e.g., POPC), sphingomyelin, and cholesterol: 1) significantly enhanced permeability for glucose (but not sucrose) and 2) large-scale liquid-liquid phase separation of membrane molecules producing janus-like membrane morphologies. To our knowledge, a novel interplay of these biophysical properties—namely, a coupling of physical forces at the boundaries of phase-separated domains (i.e., line tension) with the elevated membrane permeability—governs the behaviors of plant lipid containing giant vesicles to osmotic stresses. These are discussed in turn below.

Line-tension-dependent domain organization in plant lipid vesicles

In this work, we reconstituted dominant plant plasma membrane lipids—namely Soy-PC, Sito, and GlcCer—in GUVs and first characterized their lateral organization. We found that these membranes display a striking lateral phase separation into sterol-enriched L_o-like and sterol-depleted L_d-like phases characterized by a single, macroscopic domain. The emergence of domain morphology naturally gives rise to phase boundaries, which accrue positive free energy per unit length at the domain edges in the form of line tension (σ, J/m). The latter originates from the differences in molecular thickness of the coexisting domains (or hydrophobic mismatch) as well as accompanying elastic distortions (i.e., oscillatory height profile due to local lipid tilt and splay) near the domain edge (51). At the simplest level, the magnitude of this line tension determines the properties of the phase-separated domains, including size, number, and curvature. Theoretical models predict that the line tension scales quadratically with the height mismatch and that, on average, a height mismatch between domain and surrounding membrane of 3 Å generates $\sim 1 \times 10^{-12}$ J/m (or 1 pN) line tension (51). Consistent with this prediction, experimental estimates of line tension at the domain boundaries for a range of ternary lipid mixtures containing cholesterol and sphingomyelin have been shown to range from 0.06×10^{-12} to 6×10^{-12} J/m (0.06–6 pN) depending on the height mismatch (52). As a consequence of this elastic interfacial energy stored at the domain edges, the minimization of the boundary length is thermodynamically favored, providing a driving force for a large-scale segregation of coexisting phases into single, macroscopic domains such as we observe. In general, this tendency for macroscopic phase separation in lipid bilayers is opposed by differences in the physical properties of the coexisting phases including bending energy, spontaneous curvature, and Gaussian curvature, as revealed by continuum theoretical models (53) and confirmed by experiments (29,52,54) and molecular dynamics simulations (55). In addition, nonequilibrium scenarios in which domain coarsening is kinetically arrested because of high viscosity of the membrane (56) also play a role in stabilizing the multidomain morphologies observed in the typical models used to characterize mammalian plasma membranes (57,58). Our observations that the Soy-PC/Sito/GlcCer membranes produce single, large, microscopic domains are thus consistent with the picture in which the two coexisting L_o-like and L_d-like phases do not differ substantially in their spontaneous curvatures or bending rigidities

(including Gaussian curvatures) and that the phase boundary forces due to line tension act as the primary determinant of the domain morphology (52).

Osmotically mediated vesicle deformations reflect an interplay of membrane permeability and line tension

The results presented here reveal an unusual osmotic response of GUVs containing plant plasma membrane lipids. When subjected to hypertonic stress from the surrounding bath, they exhibit a bimodal response characterized by a plastic deformation involving budding and division in one case and a reversible, elastic deformation characterized by the transitory appearance of a domain-induced bud in the other. Analyzing these findings reveals an intriguing interplay of selective solute permeabilities and monodomain morphologies of plant lipid membranes, as discussed below.

First, a common feature of osmotically induced deformation in all cases above is the stochastic appearance of the characteristic domain-induced budding, which directly implicates the changing interplay between the phase boundary forces and curvature energy. Recall a theoretical treatment by Jülicher and Lipowsky (59,60), which establishes that the line tension σ at the domain boundaries scales with the length of the domain boundary, but the energetic penalty for bending—namely curvature energy, determined by bending rigidity (κ)—is size invariant. Because the bending of the domain reduces the boundary length and thus lowers the edge energy, budding sets a competition in which the balance of reduction in line tension and the gain in the curvature energy determines equilibrium shape. Thus, above a threshold domain size—the length scale of which is set by the ratio of bending and edge energies, $\xi = (\kappa/\sigma)$—bud formation becomes energetically favorable (59). Assuming an approximate value of κ of $\sim 4 \times 10^{-19}$ J for a typical lipid-sterol mixture in the fluid phase and a line tension σ of $\sim 1 \times 10^{-12}$ J/m, the characteristic invagination length is estimated at $\xi \cong 400$ nm, which is much smaller than the domain sizes we observe. This local mechanism for membrane budding, however, is opposed by the global constraints on the vesicle volume. When the reduced volume—$v = V/[4\pi R_0^3/3]$, where R_0 corresponds to the radius of an equivalent sphere of area $S = [4\pi R_O^2]$—is ~ 1 and the vesicle essentially spherical, the tendency for domain-induced budding is strongly suppressed, such as we observe with isotonic GUVs (Fig. 1). But when the $v = 1$ constraint is lifted, such as during osmotic deflation induced by an applied hypertonic stress, the competition between line tension and curvature energy promotes budding below the critical reduced volume. The critical reduced volume is given by the minimal energy shape of two complete spheres (60), each corresponding to the size of the L_o-like and the L_d-like phases, connected by an infinitesimal neck: $v_{sp} \equiv [V^{(L_O)} + V^{(L_D)}]/[4\pi R_0^3/3] = (1-x)^{3/2} + x^{3/2}$, where x corresponds to the relative domain area, $A^{(L_D)}/[A^{(L_O)} + A^{(L_D)}]$. In this case, the fraction of solvent removed from the vesicle interior because of the applied osmotic pressure gradient corresponding to $\Delta c = 200$ mM yields $v \approx 0.6$, which is lower than the minimum $v_{sp} \approx 1/\sqrt{2}$, enabling the domain-induced budding transition that we observe.

Second, the direction of budding is invariably outward. The notion that sterols determine the directionality of budding has been previously proposed (29) by considering the flip-flop rates of sterols between the membrane leaflets within the theoretical framework of the spontaneous curvature model (60). This model predicts that the outward budding, which generates positive membrane curvatures, relieves membrane tension readily if the needed increase in the area of the outer leaflet is met. The latter can be readily met in our membranes because the flip-flop rates of cholesterol and Sito with only one hydroxyl group as a polar moiety are fast (half-life, <1 s) (61,62) and because sterols lower the activation free-energy barrier for lipid flip-flop (63). An alternate possibility that we cannot rule out is that the outward flux of water during osmotic deflation can redistribute some lipids from the inner to the outer leaflet of the bilayer, leading to an area asymmetry between the membrane leaflets and stabilizing bud-generating spontaneous curvatures (60).

Third, and perhaps the most intriguing aspect of the vesicular response to the imposed hypertonic stress, is the observation of reversible budding in roughly 70% of the cases. The reversibility in budding requires a dramatic flip in the directionality of the osmotic stress. Immediately after the application of the hypertonic stress, the removal of water from the vesicular interior increases the area/volume ratio. The excess membrane area then paves for budding, such as we first witness. The abrupt reversal in the budding dynamics, however, suggests a delayed reintroduction of water into the vesicles requiring solute concentration difference to switch sign (upshift to downshift), which can be reconciled in terms of the dynamics of permeable glucose, as proposed below.

The plant lipid GUVs, as prepared, are filled with an aqueous solution of impermeable sucrose and surrounded by an isotonic solution of sucrose. Under this condition of equal colligative potential, there is no net osmotic activity. When the extravesicular medium is exchanged for a solution containing membrane-permeable glucose, the concentration gradient due to diffusible glucose drives the solute into the vesicle altering the osmotic balance and inducing an osmotically driven, net water influx. Indeed, this movement of glucose subjects even isotonic GUVs to hopotonic stress when sucrose-containing GUVs are placed in glucose solution. Similar observations of osmotic swelling due to directional movement of permeable solutes have been previously reported, albeit in different contexts (43,64). Perhaps one of

the most striking realizations of this behavior occurs when glucose containing GUVs are embedded in a hypotonic solution containing sucrose osmolyte. Here, the slow permeation of glucose from the vesicle interior gradually transforms the initial hypotonic exterior into a hypertonic one. The timescale for this reversal is determined by the membrane permeability and thus the characteristic permeation time (~9 min) for diffusion of glucose. This reversal in the osmotic imbalance then transforms an initially swelling GUV into a budding one, reflecting a lowered volume/area ratio (Supporting Materials and Methods; Fig. S4; Video S16)

In this same vein, when GUVs are immersed in the hypertonic exterior containing higher concentrations of glucose, two distinct but inter-related transport processes set in: 1) hypertonic stress tending to drive the solvent out of the GUV and 2) the transvesicular glucose concentration gradient driving the permeable solute into the GUV. Because membrane permeability for water is high and corresponding relaxation time low (<1 s), efflux of water from the interior of GUV commences instantaneously. As a result, the GUV deforms at the phase boundary, giving rise to the characteristic domain-induced budding such as we observe. Concomitantly, the removal of water also elevates the effective sucrose concentration inside the GUV, reducing the solute concentration difference across the vesicle. With the passage of time, however, the slower permeation of glucose into the interior of the GUV (relaxation time ~400 s) begins to accrue glucose molecules inside the vesicular interior, producing a reversal in the direction of the osmotic stress. This in turn decreases the excess membrane area relative to the encapsulated volume, creating an unusual situation in which the incipient bud returns to the mother vesicle, reconstituting the starting mother vesicle configuration.

CONCLUSIONS

In summary, the results presented here reveal new roles, to our knowledge, for the lipid composition of plant plasma membranes in determining their lateral organization and responsiveness to the applied osmotic stress. Faced with constant assault from osmotic stresses, it is now well appreciated that plants promote their growth and development by tightly controlling water transport at the level of single cells (65). Although this water regulation is afforded by the spatial compartmentalization of the cellular milieu into vacuole and cytoplasm, how the movement of water across the membrane interface is regulated has remained largely elusive. The results presented here support the idea that by employing PUFA-laden lipids and dynamically organizing them into membrane domains, plant membranes not only achieve high effective permeability for water but also control water-stress-induced and domain-boundary-mediated membrane deformations. This interplay of elevated membrane permeability, line-tension-mediated physical forces, and conformational adaptability—we speculate—affords the PUFA-containing phospholipid membranes a control mechanism and a "kinetic" advantage in managing osmotic stresses; it drives segregation of molecules enriching deformed buds with specific molecules and allows membranes to reverse the course of budding, thus minimizing material turnover due to frequent water stresses experienced by plasma membranes of higher plants and possibly specialized membranes in other species enriched in PUFA-containing phospholipids.

The authors declare that the main data supporting the findings of this study are available within the article and its Supporting Material file. Extra data are available from the corresponding author (A.N.P.) upon request.

SUPPORTING MATERIAL

Supporting Materials and Methods, seven figures, and 16 videos are available at http://www.biophysj.org/biophysj/supplemental/S0006-3495(18)31114-7.

AUTHOR CONTRIBUTIONS

S.E. designed and performed the first round of experiments, analyzed data, and wrote the first draft of the manuscript. W.-C.S. carried out additional rounds of experiments, contributed new experiments on osmotic stress response, performed statistics, and analyzed data. S.P. carried out vesicle permeability measurements using phase-contrast microscopy, analyzed data, and wrote the corresponding sections of the manuscript. V.N.N. contributed protocols for GUV preparation and coperformed initial experiments. A.N.P. conceived the research, supervised the study, designed experiments, and wrote the manuscript. All authors discussed the results, edited the manuscript, and agree with the final content.

ACKNOWLEDGMENTS

This work is supported by a grant from Physics of Living Systens, National Science Foundation NSF PHY-1505017. S.P. is funded by a seed grant from Nanyang Technological University, Singapore, through the Center for Precision Biology. The 3i Marianas spinning disk confocal used in this study was purchased using National Institutes of Health Shared Instrumentation Grant 1S10RR024543-01. We thank the MCB Light Microscopy Imaging Facility, which is a UC-Davis Campus Core Research Facility, for the use of this microscope.

REFERENCES

1. Somerville, C., and J. Browse. 1991. Plant lipids: metabolism, mutants, and membranes. *Science.* 252:80–87.
2. Feller, S. E., K. Gawrisch, and A. D. MacKerell, Jr. 2002. Polyunsaturated fatty acids in lipid bilayers: intrinsic and environmental contributions to their unique physical properties. *J. Am. Chem. Soc.* 124:318–326.
3. Olbrich, K., W. Rawicz, …, E. Evans. 2000. Water permeability and mechanical strength of polyunsaturated lipid bilayers. *Biophys. J.* 79:321–327.
4. Rawicz, W., K. C. Olbrich, …, E. Evans. 2000. Effect of chain length and unsaturation on elasticity of lipid bilayers. *Biophys. J.* 79:328–339.

5. Antonny, B., S. Vanni, …, T. Ferreira. 2015. From zero to six double bonds: phospholipid unsaturation and organelle function. *Trends Cell Biol.* 25:427–436.
6. Barelli, H., and B. Antonny. 2016. Lipid unsaturation and organelle dynamics. *Curr. Opin. Cell Biol.* 41:25–32.
7. Pinot, M., S. Vanni, …, H. Barelli. 2014. Lipid cell biology. Polyunsaturated phospholipids facilitate membrane deformation and fission by endocytic proteins. *Science.* 345:693–697.
8. Mahajan, S., and N. Tuteja. 2005. Cold, salinity and drought stresses: an overview. *Arch. Biochem. Biophys.* 444:139–158.
9. Carpita, N., D. Sabularse, …, D. P. Delmer. 1979. Determination of the pore size of cell walls of living plant cells. *Science.* 205:1144–1147.
10. Hou, Q., G. Ufer, and D. Bartels. 2016. Lipid signalling in plant responses to abiotic stress. *Plant Cell Environ.* 39:1029–1048.
11. Haswell, E. S., and P. E. Verslues. 2015. The ongoing search for the molecular basis of plant osmosensing. *J. Gen. Physiol.* 145:389–394.
12. Ferrando, M., and W. E. L. Spiess. 2001. Cellular response of plant tissue during the osmotic treatment with sucrose, maltose, and trehalose solutions. *J. Food Eng.* 49:115–127.
13. Oparka, K. J. 1994. Plasmolysis - new insights into an old process. *New Phytol.* 126:571–591.
14. Kinnunen, P. K. J. 2000. Lipid bilayers as osmotic response elements. *Cell. Physiol. Biochem.* 10:243–250.
15. Yuan, F., H. Yang, …, Z. M. Pei. 2014. OSCA1 mediates osmotic-stress-evoked Ca^{2+} increases vital for osmosensing in Arabidopsis. *Nature.* 514:367–371.
16. Hamilton, E. S., G. S. Jensen, …, E. S. Haswell. 2015. Mechanosensitive channel MSL8 regulates osmotic forces during pollen hydration and germination. *Science.* 350:438–441.
17. Homann, U. 1998. Fusion and fission of plasma-membrane material accommodates for osmotically induced changes in the surface area of guard-cell protoplasts. *Planta.* 206:329–333.
18. Hartmann, M. A. 1998. Plant sterols and the membrane environment. *Trends Plant Sci.* 3:170–175.
19. Michaelson, L. V., J. A. Napier, …, J. D. Faure. 2016. Plant sphingolipids: their importance in cellular organization and adaption. *Biochim. Biophys. Acta.* 1861:1329–1335.
20. Grosjean, K., S. Mongrand, …, P. Gerbeau-Pissot. 2015. Differential effect of plant lipids on membrane organization: specificities of phytosphingolipids and phytosterols. *J. Biol. Chem.* 290:5810–5825.
21. Angelova, M. I., and D. S. Dimitrov. 1986. Liposome electroformation. *Faraday Discuss.* 81:303–311.
22. Morales-Penningston, N. F., J. Wu, …, G. W. Feigenson. 2010. GUV preparation and imaging: minimizing artifacts. *Biochim. Biophys. Acta.* 1798:1324–1332.
23. Kang, M., C. A. Day, …, E. DiBenedetto. 2012. Simplified equation to extract diffusion coefficients from confocal FRAP data. *Traffic.* 13:1589–1600.
24. Menger, F. M., and M. I. Angelova. 1998. Giant vesicles: imitating the cytological processes of cell membranes. *Acc. Chem. Res.* 31:789–797.
25. Cacas, J. L., F. Furt, …, S. Mongrand. 2012. Lipids of plant membrane rafts. *Prog. Lipid Res.* 51:272–299.
26. Furt, F., F. Simon-Plas, and S. Mongrand. 2011. Lipids of the plant plasma membrane. The Plant Plasma Membrane. Springer, pp. 3–30.
27. Lee, W. J., S. H. Weng, and N. W. Su. 2015. Individual phosphatidylcholine species analysis by RP-HPLC-ELSD for determination of polyenylphosphatidylcholine in lecithins. *J. Agric. Food Chem.* 63:3851–3858.
28. Baumgart, T., G. Hunt, …, G. W. Feigenson. 2007. Fluorescence probe partitioning between Lo/Ld phases in lipid membranes. *Biochim. Biophys. Acta.* 1768:2182–2194.
29. Bacia, K., P. Schwille, and T. Kurzchalia. 2005. Sterol structure determines the separation of phases and the curvature of the liquid-ordered phase in model membranes. *Proc. Natl. Acad. Sci. USA.* 102:3272–3277.
30. Brzustowicz, M. R., V. Cherezov, …, S. R. Wassall. 2002. Molecular organization of cholesterol in polyunsaturated membranes: microdomain formation. *Biophys. J.* 82:285–298.
31. Veatch, S. L., and S. L. Keller. 2003. Separation of liquid phases in giant vesicles of ternary mixtures of phospholipids and cholesterol. *Biophys. J.* 85:3074–3083.
32. Baumgart, T., A. T. Hammond, …, W. W. Webb. 2007. Large-scale fluid/fluid phase separation of proteins and lipids in giant plasma membrane vesicles. *Proc. Natl. Acad. Sci. USA.* 104:3165–3170.
33. Purushothaman, S., J. Cama, and U. F. Keyser. 2016. Dependence of norfloxacin diffusion across bilayers on lipid composition. *Soft Matter.* 12:2135–2144.
34. Faure, C., F. Nallet, …, O. Lambert. 2006. Modeling leakage kinetics from multilamellar vesicles for membrane permeability determination: application to glucose. *Biophys. J.* 91:4340–4349.
35. Papahadjopoulos, D., S. Nir, and S. Oki. 1972. Permeability properties of phospholipid membranes: effect of cholesterol and temperature. *Biochim. Biophys. Acta.* 266:561–583.
36. Jung, C. Y. 1971. Permeability of bimolecular membranes made from lipid extracts of human red cell ghosts to sugars. *J. Membr. Biol.* 5:200–214.
37. Haleva, E., and H. Diamant. 2008. Critical swelling of particle-encapsulating vesicles. *Phys. Rev. Lett.* 101:078104.
38. Peterlin, P., V. Arrigler, …, H. Diamant. 2012. Law of corresponding states for osmotic swelling of vesicles. *Soft Matter.* 8:2185–2193.
39. Ertel, A., A. G. Marangoni, …, J. M. Wood. 1993. Mechanical properties of vesicles. I. Coordinated analysis of osmotic swelling and lysis. *Biophys. J.* 64:426–434.
40. Mui, B. L., P. R. Cullis, …, T. D. Madden. 1993. Osmotic properties of large unilamellar vesicles prepared by extrusion. *Biophys. J.* 64:443–453.
41. Su, W. C., D. L. Gettel, …, A. N. Parikh. 2018. Pulsatile gating of giant vesicles containing macromolecular crowding agents induced by colligative nonideality. *J. Am. Chem. Soc.* 140:691–699.
42. Oglęcka, K., P. Rangamani, …, A. N. Parikh. 2014. Oscillatory phase separation in giant lipid vesicles induced by transmembrane osmotic differentials. *eLife.* 3:e03695.
43. Peterlin, P., and V. Arrigler. 2008. Electroformation in a flow chamber with solution exchange as a means of preparation of flaccid giant vesicles. *Colloids Surf. B Biointerfaces.* 64:77–87.
44. Koslov, M. M., and V. S. Markin. 1984. A theory of osmotic lysis of lipid vesicles. *J. Theor. Biol.* 109:17–39.
45. Reigada, R. 2014. Electroporation of heterogeneous lipid membranes. *Biochim. Biophys. Acta.* 1838:814–821.
46. Sengel, J. T., and M. I. Wallace. 2016. Imaging the dynamics of individual electropores. *Proc. Natl. Acad. Sci. USA.* 113:5281–5286.
47. Baumgart, T., S. T. Hess, and W. W. Webb. 2003. Imaging coexisting fluid domains in biomembrane models coupling curvature and line tension. *Nature.* 425:821–824.
48. Duwe, H. d., and E. Sackmann. 1990. Bending elasticity and thermal excitations of lipid bilayer vesicles: modulation by solutes. *Physica A.* 163:410–428.
49. Sankhagowit, S., E. Y. Lee, …, N. Malmstadt. 2016. Oxidation of membrane curvature-regulating phosphatidylethanolamine lipid results in formation of bilayer and cubic structures. *Langmuir.* 32:2450–2457.
50. Moroz, J. D., P. Nelson, …, E. Moses. 1997. Spontaneous expulsion of giant lipid vesicles induced by laser tweezers. *Phys. Rev. Lett.* 78:386–389.
51. Kuzmin, P. I., S. A. Akimov, …, F. S. Cohen. 2005. Line tension and interaction energies of membrane rafts calculated from lipid splay and tilt. *Biophys. J.* 88:1120–1133.
52. García-Sáez, A. J., S. Chiantia, and P. Schwille. 2007. Effect of line tension on the lateral organization of lipid membranes. *J. Biol. Chem.* 282:33537–33544.

53. Elson, E. L., E. Fried, …, G. M. Genin. 2010. Phase separation in biological membranes: integration of theory and experiment Annu. Rev. Biophys. 39:207–226.

54. Ursell, T. S., W. S. Klug, and R. Phillips. 2009. Morphology and interaction between lipid domains. *Proc. Natl. Acad. Sci. USA.* 106:13301–13306.

55. Hu, J. L., T. R. Weikl, and R. Lipowsky. 2011. Vesicles with multiple membrane domains. *Soft Matter.* 7:6092–6102.

56. Frolov, V. A., Y. A. Chizmadzhev, …, J. Zimmerberg. 2006. "Entropic traps" in the kinetics of phase separation in multicomponent membranes stabilize nanodomains. *Biophys. J.* 91:189–205.

57. Schmid, F. 2017. Physical mechanisms of micro- and nanodomain formation in multicomponent lipid membranes. *Biochim. Biophys. Acta Biomembr.* 1859:509–528.

58. Yanagisawa, M., M. Imai, …, T. Ohta. 2007. Growth dynamics of domains in ternary fluid vesicles. *Biophys. J.* 92:115–125.

59. Jülicher, F., and R. Lipowsky. 1993. Domain-induced budding of vesicles. *Phys. Rev. Lett.* 70:2964–2967.

60. Jülicher, F., and R. Lipowsky. 1996. Shape transformations of vesicles with intramembrane domains. *Phys. Rev. E Stat. Phys. Plasmas Fluids Relat. Interdiscip. Topics.* 53:2670–2683.

61. Steck, T. L., J. Ye, and Y. Lange. 2002. Probing red cell membrane cholesterol movement with cyclodextrin. *Biophys. J.* 83:2118–2125.

62. Allhusen, J. S., and J. C. Conboy. 2017. The ins and outs of lipid flip-flop. *Acc. Chem. Res.* 50:58–65.

63. Allhusen, J. S., D. R. Kimball, and J. C. Conboy. 2016. Structural origins of cholesterol accelerated lipid flip-flop studied by sum-frequency vibrational spectroscopy. *J. Phys. Chem. B.* 120:3157–3168.

64. Mally, M., J. Majhenc, …, B. Žekš. 2002. Mechanisms of equinatoxin II-induced transport through the membrane of a giant phospholipid vesicle. *Biophys. J.* 83:944–953.

65. Zonia, L., and T. Munnik. 2007. Life under pressure: hydrostatic pressure in cell growth and function. *Trends Plant Sci.* 12:90–97.